A Numerical Study of Smoke Concentration Distribution near Low-Intensity Fires: Sensitivity to Vertical Canopy Structure and Fire Heat Source Strength

MICHAEL T. KIEFER,[a] SHIYUAN ZHONG,[a] JOSEPH J. CHARNEY,[b] XINDI BIAN,[b] WARREN E. HEILMAN,[b] AND JOSEPH SEITZ[a]

[a] *Department of Geography, Environment, and Spatial Sciences, Michigan State University, East Lansing, Michigan*
[b] *USDA Forest Service, Northern Research Station, East Lansing, Michigan*

(Manuscript received 21 September 2023, in final form 7 March 2024, accepted 25 April 2024)

ABSTRACT: Broadly speaking, prediction of the negative impacts of prescribed fire on air quality is limited by gaps in our understanding of the underlying fire, fuels, and atmospheric processes. These knowledge gaps hinder our ability to accurately predict smoke concentration distributions, leading to unintended smoke intrusions into nearby communities and subsequent threats to public health and safety. In this study, numerical simulations are performed using the Flexible Particle Weather Research and Forecasting (FLEXPART-WRF) Model, a Lagrangian particle dispersion model, with particle motion driven by output from a full-physics atmospheric model with a forest canopy submodel and 10-m horizontal grid spacing [Advanced Regional Prediction System (ARPS)-CANOPY], to address two research questions. First, what is the relationship between near-fire (within ~50–150 m of fire) smoke concentration distribution and (i) vertical canopy structure and (ii) fire heat source strength? Second, what roles do mean transport (i.e., transport by the mean wind) and turbulent diffusion play in shaping the near-fire smoke concentration distribution? To address these questions, simulations are run with 25 combinations of plant area density profile and fire sensible heat flux magnitude, and smoke is represented by particles with diameters $\leq 2.5\ \mu$m ($PM_{2.5}$). Results show that near-fire $PM_{2.5}$ concentration distribution is primarily controlled by vertical canopy structure, with fire heat source strength primarily controlling the $PM_{2.5}$ concentration magnitude. Analysis of the underlying ARPS-CANOPY variables driving the FLEXPART-WRF particle dispersion helps elucidate the roles of mean transport and turbulent diffusion. In total, the study findings suggest that the vertical distribution of canopy vegetation and fire heat source strength are important factors influencing $PM_{2.5}$ dispersion and concentration distribution near low-intensity fires.

KEYWORDS: Atmosphere; Forest canopy; Dispersion; Turbulence; Forest fires; Air quality

1. Introduction

Prescribed fire is a tool used by public and private land managers to accomplish forest and agricultural land management goals (e.g., hazardous fuel reduction, forest health and restoration, and wildlife habitat management). Between 2000 and 2019, more than 1 million prescribed fires burning more than 24 million ha were conducted in the United States (U.S.) (National Interagency Fire Center 2019). Furthermore, a recently released 10-yr strategy calls for the U.S. Forest Service (USFS) to treat up to an additional 8 million ha of national forests and grasslands (using prescribed fires and mechanical thinning) and to support treatment of up to an additional 12 million ha of other Federal, State, Tribal, private, and family lands (USFS 2022).

A by-product of fire is smoke generated from incomplete combustion (van Wagtendonk 2006). Although smoke from high-intensity wildfires can have impacts on regional and continental scales, smoke from low-intensity prescribed fires does not generally have such large-scale impacts; nevertheless, on the local scale, the effects can be substantial. Smoke from prescribed fires can have a direct effect on public health and safety in nearby communities, as well as the health and safety of operational fire management personnel, mainly through air quality and visibility degradation (Lahm 2020). In fact, negative public perception of smoke impacts has been identified as a possible impediment to prescribed fire use on public lands (Ryan et al. 2013; Engebretson et al. 2016). Because air quality and visibility issues occur more often when smoke concentrations are high, smoke prediction products (e.g., particulate concentration forecasts) are an important component of the suite of tools used by land management personnel for decision-making regarding planned burns [e.g., BlueSky (Larkin et al. 2009); QUIC-Fire (Linn et al. 2020)].

Broadly speaking, the prediction of the negative impacts of prescribed fire on air quality is limited by gaps in our understanding of the underlying fire, fuels, and atmospheric processes, and their complex interactions (Hiers et al. 2020; Jaffe et al. 2020). The lack of understanding of these processes contributes to inaccurate predictions of smoke concentration distributions and in some cases unintended smoke intrusions into nearby communities, threatening public health and safety (Miller et al. 2019). Predicting the local distribution of smoke from low-intensity prescribed fires is challenging because the underlying dispersion processes are sensitive to environmental factors such as near-surface meteorological conditions (including fire-induced meteorological conditions), local topography,

Supplemental information related to this paper is available at the Journals Online website: https://doi.org/10.1175/JAMC-D-23-0173.s1.

Corresponding author: Michael T. Kiefer, mtkiefer@msu.edu

DOI: 10.1175/JAMC-D-23-0173.1

forest overstory vegetation, and atmospheric turbulence within and above vegetation layers, in addition to fuels, the time of day when the fire is ignited, and the pattern of ignition (Liu et al. 2018, 2019; Hiers et al. 2020). As a point of clarification, the term "dispersion" is used herein to refer to the movement of particles or gases by a combination of mean transport (i.e., transport by the mean wind) and turbulent diffusion [in the context of this numerical study, diffusion by a combination of grid-resolved and subgrid-scale (SGS) turbulent eddies].

This study aims to address two research questions regarding the distribution of smoke from low-intensity prescribed fires in forested environments. First, what is the relationship between near-fire smoke concentration distribution and (i) vertical canopy structure and (ii) fire heat source strength? The term "near-fire" is used in this study to refer to the area of the overlying atmosphere within about 50–150 m (~3–10 canopy heights) of a low-intensity surface fire. This is the same area of the atmosphere analyzed in the Kiefer et al. (2018) study of atmospheric perturbations induced by the sensible heat released from low-intensity surface fires. Second, what roles do mean transport and turbulent diffusion play in shaping the near-fire smoke concentration distribution? To help answer these questions, the Flexible Particle Weather Research and Forecasting Model (FLEXPART-WRF, version 3.3; Brioude et al. 2013), a Lagrangian particle dispersion model, is used to simulate particulate matter dispersion using meteorological output from a full-physics atmospheric model with a forest canopy submodel [Advanced Regional Prediction System (ARPS)-CANOPY, version 5.2.12; Kiefer et al. 2013, 2018].

Knowledge of the distribution of smoke concentration in the near-fire area, particularly the tendency of smoke to either remain within the forest canopy or move out of the canopy, may help inform studies of smoke concentration distribution across deeper layers of the atmosphere and the associated local- to regional-scale dispersion. Thus, although this study focuses on smoke distributions over smaller distances than those generally separating prescribed fires from nearby communities (on the order of kilometers or more), the study findings are expected to have implications beyond the near-fire area. Near-fire smoke dispersion and concentration distribution are pieces of a much larger puzzle of smoke plume dynamics that includes, for example, smoke emissions, plume rise, plume entrainment and detrainment, and moist thermodynamics (Liu et al. 2022). The focus on near-fire smoke concentration distribution [as opposed to distribution through the planetary boundary layer (PBL) and overlying free atmosphere] is further motivated by the use of ARPS-CANOPY output from Kiefer et al. (2018), with physical domain dimensions on the order of 1 km^3 and a horizontal grid spacing of 10 m, to drive particle dispersion in FLEXPART-WRF. Additionally, the application in Kiefer et al. (2018) of a fire sensible heat source extending the length of the model domain in the south–north direction necessitates our focus on cross-fireline (as opposed to along-fireline) horizontal smoke concentration distribution.

The study is organized as follows: section 2 describes the study methodology, including descriptions of the ARPS-CANOPY model and FLEXPART-WRF Model (section 2a), the model configurations and design of numerical experiments (section 2b), and the analysis methodology (section 2c); section 3 presents the study results and discussion, consisting of the analysis of the simulated FLEXPART-WRF particulate matter concentration (section 3a) and ARPS-CANOPY meteorological variables driving FLEXPART-WRF particle dispersion (section 3b), and the paper is concluded in section 4.

2. Materials and methods

a. *Model description*

1) ARPS-CANOPY

ARPS-CANOPY is a version of the ARPS model (Xue et al. 2000, 2001) that includes a canopy submodel in which the effects of vegetation elements on drag, turbulence production/dissipation, radiation transfer, and the surface energy budget are accounted for through modifications to the original ARPS model equations and physical parameterizations (Kiefer et al. 2013). Such changes allow for the explicit simulation of the mean and turbulent airflow through a multilevel forest canopy. At each grid point, a vertical profile of plant area density A_p, defined as the one-sided area of plant material per unit volume, is utilized to represent the bulk effects of the canopy on atmospheric processes (e.g., canopy drag and ground shading). For a more complete description of ARPS-CANOPY, see Kiefer et al. (2013).

A 1.5-order local turbulence parameterization (Deardorff 1980; Moeng and Wyngaard 1989) is utilized in ARPS-CANOPY, with a prognostic equation for SGS turbulent kinetic energy (TKE) that includes canopy source and sink terms. In all simulations, the original ARPS anisotropic turbulence option is used in which both horizontal and vertical components of eddy viscosity and diffusivity are computed; this option is recommended when vertical grid spacing is considerably smaller than horizontal grid spacing (Xue et al. 2000). This SGS turbulence parameterization has been tested extensively and has been found to produce the correct vertical structure of mean variables and turbulent statistics with and without a forest canopy (e.g., Dupont and Brunet 2008; Kiefer et al. 2013, 2014, 2022). Furthermore, ARPS-CANOPY utilizes a land surface model based on Noilhan and Planton (1989) and Pleim and Xiu (1995) and radiation physics following Chou (1990, 1992) and Chou and Suarez (1994), with the addition of canopy shading effects on the surface energy budget in the former and a canopy heat source/sink term in the latter.

2) FLEXPART-WRF

FLEXPART-WRF (Brioude et al. 2013) is a version of the Lagrangian particle dispersion model FLEXPART (Stohl et al. 2005; Pisso et al. 2019), originally developed for use with global weather models, that has been adapted for use with limited-area models, specifically the WRF Model (Powers et al. 2017). Although we refer to the model by its proper name "FLEXPART-WRF," in this study, the meteorological variables used by FLEXPART-WRF originate from the ARPS-CANOPY model output, as in Charney et al. (2019). In that study, the authors concluded from a comparison of smoke plume simulations and field observations during a low-intensity fire that the model was capable of reproducing some, but not all, of the spatiotemporal variability of observed surface smoke concentrations and plume heights, with differences attributed to shortcomings of the model representation of the fire sensible heat source as well as unresolved smoke gradients. Additionally, FLEXPART-WRF simulations driven by the output from the original ARPS have been used to study smoke dispersion in complex terrain in eastern Pennsylvania (Kiefer et al. 2019) and southwestern Colorado (Kiefer et al. 2020). Although the aforementioned FLEXPART-WRF studies have utilized horizontal grid spacing in the range of 100–400 m, Solomos et al. (2015) argued that FLEXPART-WRF has no inherent spatial-scale limitations and can be driven by output from a meteorological model with horizontal grid spacing as fine as several meters. As will be discussed in section 2b(1), the ARPS-CANOPY simulations used to drive FLEXPART-WRF particle motion in this study utilize 10-m horizontal grid spacing, approximately an order of magnitude finer than that of Kiefer et al. (2019, 2020) and closer to the lower range of grid spacing suggested by Solomos et al. (2015).

FLEXPART-WRF uses a Lagrangian reference frame, tracking individual particles and updating particle position at every time step based on grid-resolved and parameterized wind components. The grid-resolved wind component ingested by FLEXPART-WRF drives particle motion via mean transport and, for meteorological model grid spacing fine enough to resolve at least some scales of turbulence, grid-resolved turbulent diffusion. The parameterized wind component consists entirely of SGS turbulence and drives particle motion via SGS turbulent diffusion. The three-dimensional components of the grid-resolved wind (u, v, and w) are ingested from the meteorological model, with the user given the choice of using instantaneous winds, time-averaged winds, or instantaneous horizontal wind components with a diagnostic calculation of vertical velocity. Since ARPS-CANOPY does not output time-averaged winds (as in WRF versions 3.3 or higher), instantaneous winds are utilized in this study to drive FLEXPART-WRF particle motion.

The parameterized wind component is computed in FLEXPART-WRF via either the Hanna turbulence parameterization (Hanna 1982) or as a function of SGS TKE read in from the meteorological model. Brioude et al. (2013) recommended the former, based on their assessment that the ingested TKE option violates the well-mixed criterion, which dictates that an initially uniform distribution of particles in an incompressible flow should remain uniform during the Lagrangian model simulation (Bahlali et al. 2020). Although Charney et al. (2019) and Kiefer et al. (2019, 2020) followed the recommendation of Brioude et al. (2013) and used the Hanna turbulence formulation, we choose here to use the SGS TKE read in from ARPS-CANOPY to compute the parameterized wind component for three reasons. First, the incompressibility constraint (Brioude et al. 2013; Bahlali et al. 2020) is unquestionably violated in this study, given the focus on atmospheric phenomena with spatial scales on the order of 10–100 m and surface sensible heat fluxes in the range of 25–100 kW m^{-2}. Second, the WRF simulations cited by Brioude et al. (2013) in arguing against the ingested TKE option utilized 4-km horizontal grid spacing, necessitating the parameterization of all scales of turbulence, whereas the ARPS-CANOPY simulations in Kiefer et al. (2018) utilized 10-m horizontal grid spacing, implying that only turbulent eddies smaller than about 10 m in scale were parameterized. Third, sensitivity tests using the ARPS-CANOPY meteorological output and the FLEXPART-WRF Hanna formulation yielded unrealistically strong and rapid dispersion of particles throughout the model domain (not shown), similar to Cornwell et al. (2021).

The FLEXPART-WRF parameterized wind component is partitioned into its three-dimensional subcomponents (u', v', and w') via an internal routine that uses three PBL parameters ingested from the meteorological model: mixed-layer height, friction velocity, and surface heat flux. An alternate FLEXPART-WRF option to partition the parameterized wind component assuming a balance of TKE production and dissipation was deemed unsuitable since turbulent mixing of TKE is expected to be nonnegligible in the fire-perturbed atmosphere (Heilman et al. 2015). As shown in section 3b, the chosen partitioning method yields the largest parameterized wind components in the horizontal dimension. This outcome is consistent with the finding of Heilman et al. (2015) that the within-canopy turbulence regime during a low-intensity surface fire is dominated by horizontal perturbations (i.e., is anisotropic) before, during, and after fire passage.

b. *Model configuration and experiment design*

1) ARPS-CANOPY

In this study, FLEXPART-WRF particle dispersion is driven by the meteorological output from ARPS-CANOPY simulations presented in Kiefer et al. (2018). Therein, a total of 25 ARPS-CANOPY simulations were conducted with five vertical canopy structures, as represented by A_p profiles (Fig. 1), and five fire heat source strengths, as represented by sensible heat flux magnitudes in the range of 0–100 kW m^{-2}. A brief summary of the Kiefer et al. (2018) model configuration and experimental design is provided here; full details may be found in the original paper.

The Kiefer et al. (2018) ARPS-CANOPY model configuration featured two three-dimensional computational domains and a one-way nesting procedure. The outer (inner) domain simulation was initialized at 1200 (1500) local time (LT) and run for a total of 4 (1) h, with 53 × 103 × 78 (99 × 51 × 78) grid points, 50-m (10-m) horizontal grid spacing, and a periodic (one-way) lateral boundary condition. Both domains contained the same vertically stretched grid, with 40-m average and 2-m minimum vertical grid spacing at the surface, and both featured a uniform, steady net radiation flux of 520 W m^{-2} at the top of a horizontally homogeneous canopy to represent daytime heating typical of 40°N latitude in March. The primary purpose of the outer-domain simulation was to allow a quasi-horizontally homogeneous and quasi-stationary daytime convective boundary layer to develop in the absence of a fire sensible heat source. It is important to keep in mind that all simulations, with and without fire sensible heat flux, feature shear- and buoyancy-generated turbulence in the background (i.e., nonfire) atmosphere. The outer-domain simulation was initialized with a base state sounding with uniform wind

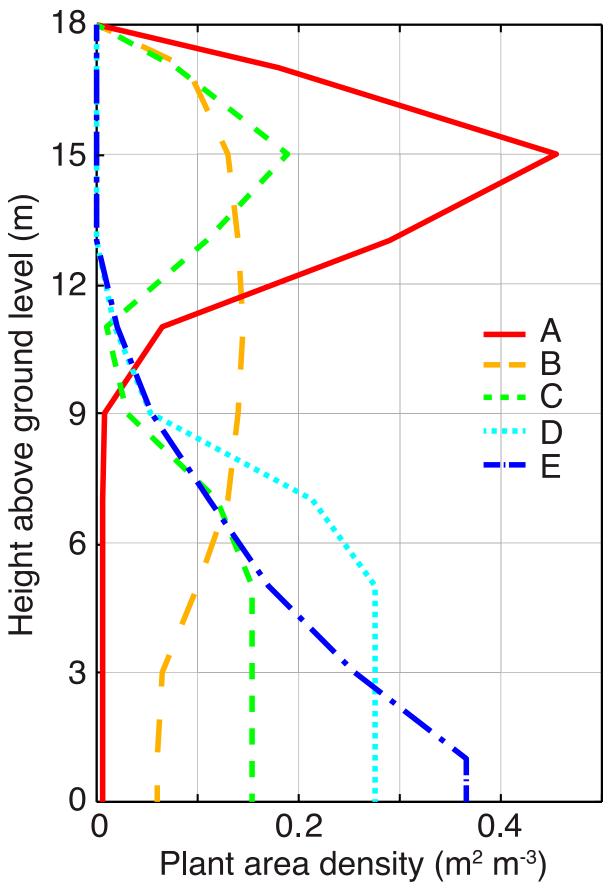

FIG. 1. Vertical profiles of plant area density A_p for the five vertical canopy structures explored in this study; note that for all canopy profiles, the plant area index (PAI) = 2 and the canopy height h = 18 m. See the main text for a description of the relationship of each profile to observed forest stands.

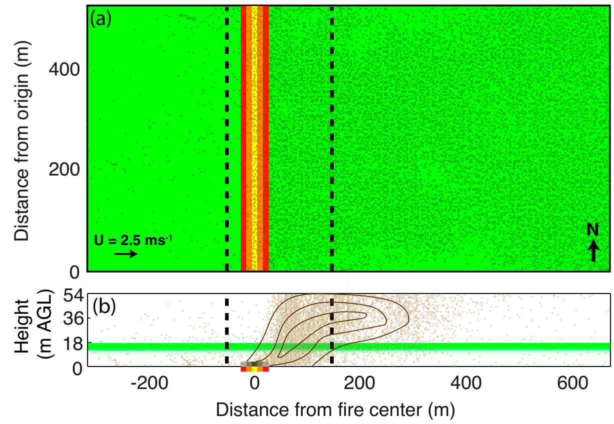

FIG. 2. Domain and fire sensible heat/$PM_{2.5}$ particle release schematic with (a) plan view and (b) vertical cross-sectional depictions of canopy and fire (Kiefer et al. (2018) and current study), and $PM_{2.5}$ particle positions and concentrations (current study only). In (a), forest is depicted with green shading, and surface heat flux in 50-m-wide strip ("fireline") is shaded from red (weakest) → yellow (strongest). In (b), a vertical cross section of plant area density in the x–z plane is provided, along with the location of the surface sensible heat flux and $PM_{2.5}$ particle release zone. Hypothetical particle positions and particle concentrations are indicated with brown dots and contours, respectively, and are intended to depict the plume appearance to observers looking (a) downward and (b) northward from positions outside of the $PM_{2.5}$ plume. Thick dashed lines denote the near-fire area displayed in subsequent figures, and the horizontal arrow in (a) denotes the initial-state vertically invariant wind speed and direction in Kiefer et al. (2018).

speed (2.5 m s^{-1}, westerly) from the surface to the domain top and neutral static stability below z = 1 km [stable stratification with the Brunt–Väisälä frequency (N) = 0.013 s^{-1} above]. Note that although a uniform westerly wind is used to initialize the outer-domain ARPS-CANOPY simulation, a combination of surface and forest canopy drag yields mean wind speeds less than 1 m s^{-1} at or below about one-half canopy height [see Fig. 7 in Kiefer et al. (2018)]. The reader is urged to keep in mind that the smoke–canopy–fire relationships examined in this study may be sensitive to the magnitude and vertical variability of the background wind; exploration of this important degree of freedom is left to future work. One-way lateral boundary conditions for the inner domain were applied every time step but updated every 5 min (i.e., output files from the outer-domain simulation were read in every 5 min).

Five A_p profiles were utilized to represent a range of vertical canopy structures, ranging from overstory-concentrated shape A, broadly representative of maritime or loblolly pine stands with dense crown layers and sparse trunk spaces, to understory-concentrated shape E, derived from light detection and ranging (lidar) measurements in a mixed pitch pine–scrub oak forest stand in New Jersey (Skowronski et al. 2011; Kiefer et al. 2014). Along with the five vertical canopy structures, five fire sensible heat flux magnitudes were applied within a 50-m-wide strip ("fireline") in the inner domain (Fig. 2a), with magnitudes varying from 0 kW m^{-2} ("no-fire") to 100 kW m^{-2}, with a 25 kW m^{-2} interval between cases. As stated in Kiefer et al. (2018), these nonzero heat flux magnitudes fall within the envelope of 1-min mean sensible heat fluxes reported during field studies of low-intensity fires [8–155 kW m^{-2} (e.g., Clements et al. 2007; Hiers et al. 2009; Heilman et al. 2015, 2021)]. The fireline was positioned 3.2 km downstream of the western lateral boundary and was applied following a 30-min spinup period. The fireline extended the length of the domain in the y direction (500 m), with the fire sensible heat flux applied for a total of 30 min and laterally distributed across the fireline in a stair-step pattern (85% of the total heat flux in the center grid point, with the remainder in the flanking cells stepping down to zero three cells away); note that the fireline was oriented perpendicular to the westerly ambient wind. The reader is urged to keep in mind that the 50-m-wide heat source utilized in Kiefer et al. (2018) is wider than what is typically found in low-intensity prescribed fires wherein the actively burning area is on the order of a few meters wide (e.g., Heilman et al. 2015) and was necessitated by the use of 10-m model grid spacing. Also, the static nature of the heat source in Kiefer et al. (2018) deviates from that of spatiotemporally varying real-world fires and was implemented to limit the degrees of freedom in that sensitivity study. The reader is encouraged to keep the limitations of the Kiefer et al. (2018) idealized modeling framework in mind when interpreting the results of the present study.

2) FLEXPART-WRF

A total of 25 FLEXPART-WRF simulations are performed in this study, with particle motion driven by the meteorological output from the Kiefer et al. (2018) ARPS-CANOPY simulations. The FLEXPART-WRF simulations are initialized at 1525 LT and run for 35 min, with a total of 300 000 particles released within the 2-m-deep lowest grid layer at a constant rate between 1530 and 1600 LT. The FLEXPART-WRF grid is consistent with the Kiefer et al. (2018) inner-domain grid, with the same horizontal and vertical grid spacings. However, the FLEXPART-WRF grid only extends to 1054.3 m above ground level (AGL), corresponding approximately to the top of the neutrally stratified atmosphere in the Kiefer et al. (2018) initial sounding, as the atmosphere above that level is omitted from most ARPS-CANOPY output files to constrain file size. ARPS-CANOPY variables are read in once every second from NetCDF files that are generated from ARPS2-FLEX, a routine that transforms the output from ARPS-CANOPY into the suite of variables that FLEXPART-WRF is designed to read in from the WRF output. Every second, three-dimensional particle position is updated and subsequently written out to an ASCII file, and particle concentration is computed within the FLEXPART-WRF grid cells. Once every minute, concentration is averaged over the last 60 instantaneous values and written out to a NetCDF file.

The 300 000 particles are released within the fireline using the same stair-step pattern used for fire sensible heat flux in Kiefer et al. (2018) (Fig. 2b), while the initial particle position within each fireline grid cell is specified randomly. The particle diameter is restricted to the range of 2.5 μm or smaller (i.e., $PM_{2.5}$), with geometric mean and minimum particle diameters of 0.5 and 0.1 μm, respectively, and a unimodal lognormal mass distribution. Given the absence of forest canopy deposition in FLEXPART-WRF, ground deposition processes are disabled. It is important to keep in mind that the particle release strategy employed in this study is idealized in nature and is not intended to represent actual emissions. The number of particles is chosen to ensure adequate particle counts for robust statistical analysis. Note that the number of particles released in FLEXPART-WRF will impact the overall magnitude, but not distribution, of particle concentration.

Before proceeding, a few words are in order regarding the purpose of the no-fire simulations in this study of $PM_{2.5}$ dispersion from low-intensity fires. The same particle release strategy is employed in the five no-fire simulations as in the 20 simulations with fire sensible heat flux. The no-fire simulations can be interpreted as depicting simulated $PM_{2.5}$ dispersion and concentration distribution in a hypothetical scenario in which the fire is weak enough that the uniform, steady net radiation flux intercepting the canopy top [section 2b(1)] is the dominant convective forcing for particle dispersion. In other words, the no-fire simulations serve as reference simulations in which the sensible heat flux from the fire is weak enough that the contribution of the fire to plume rise can be neglected.

c. *Analysis methodology*

Five variables are examined in this study: FLEXPART-WRF $PM_{2.5}$ concentration C and ARPS-CANOPY u component of the wind U, vertical velocity W, TKE E, and temperature T; the v component of the wind V is used internally by FLEXPART-WRF but is not explicitly analyzed in this study. The grid-resolved, SGS, and total components of E are expressed as E^R, E^S, and E^T, respectively. Recall that the FLEXPART-WRF parameterized wind component is derived in this study from ARPS-CANOPY E^S [section 2a(2)]. As a point of clarification, E^S is part of the standard suite of ARPS-CANOPY output variables, whereas E^R is computed from instantaneous U, V, and W as part of the postprocessing of the ARPS-CANOPY output, as in Kiefer et al. (2018):

$$E^R = \frac{1}{2}[(U - \overline{U})^2 + (V - \overline{V})^2 + (W - \overline{W})^2], \qquad (1)$$

where symbols with and without bars indicate 30-min time averages and instantaneous values, respectively, and differences represent perturbations from the mean flow.

However, caution is urged when comparing E^R in Kiefer et al. (2018) to E^R presented herein: Kiefer et al. (2018) computed E^R for each case using time averages from a no-fire simulation, regardless of whether the fire sensible heat flux was applied in that particular case or not. They argued that their E^R was not equivalent to TKE, apart from values in the no-fire simulation because the perturbations used to compute E^R (e.g., $U - \overline{U}$) contained a turbulent fluctuation component and a mean anomaly component (associated with quasi-steady fire-induced phenomena such as the updraft and surface inflow). Whereas the stated purpose of the Kiefer et al. (2018) E^R methodology was to characterize the bulk effect of the fire sensible heat flux on the hypothetical dispersion of heat, moisture, and pollutants, our aim in this dispersion modeling study is to consider the mean transport and turbulent diffusion of $PM_{2.5}$ *separately*. Thus, E^R is computed for each case using time averages and instantaneous values from the same simulation, yielding a quantity that contains only turbulent fluctuations (the mean anomaly is contained in the time average and is therefore removed). It is important to note that there is currently no consensus in the fire weather research community as to whether these quasi-steady phenomena should be classified as coherent turbulent structures (e.g., Seto et al. 2013) or as fire-induced modifications to the ambient mean flow (e.g., Kiefer et al. 2018). As this study closely follows Kiefer et al. (2018), we choose to classify these phenomena as part of the mean flow and leave further examination of this issue to future work.

All quantities are averaged over a 30-min period, encompassing the duration of fire heat flux and/or particle release. The averaging is also performed along the entire y axis, excluding the lateral boundary points in the north and south directions. This approach is justified by the quasi-two-dimensional nature of the fireline, our desire to average out individual convective boundary layer eddies, and the stated focus of this study on the cross-

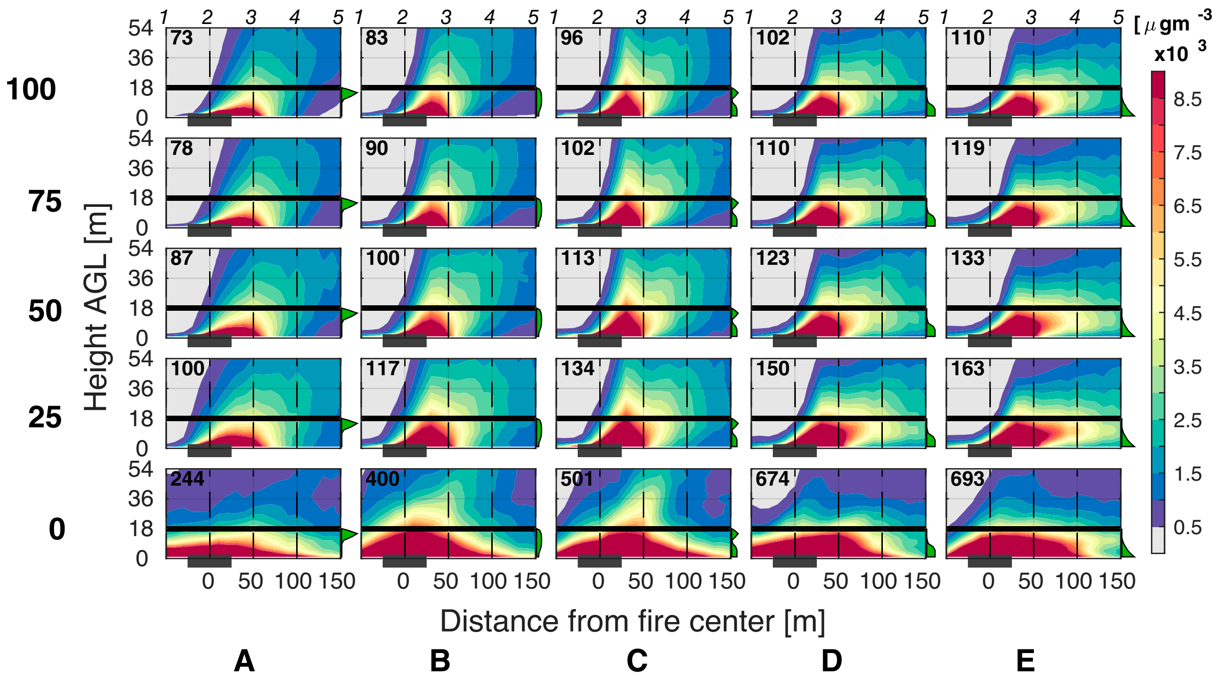

FIG. 3. Vertical cross sections of spatiotemporally averaged C [$\overline{C}_{yt}$ (y: y direction, t: 30-min); shaded] in the near-fire area (denoted by dashed lines in Fig. 2), arranged in a 5 × 5 matrix with vertical canopy structure varying between panels along the x axis (canopy profiles A–E) and fire heat flux magnitude varying between panels along the y axis (kW m^{-2}). Cross-sectional maximum $\overline{C}_{yt}$ is depicted in the upper-left corner of each panel. To conserve space, $\overline{C}_{yt}$ values are divided by 10^3. Horizontal line at 18 m denotes the canopy top, the thick black bar at the bottom of the panel depicts the fireline, and the green-filled shape to the right of the panel depicts the plant area density profile. Numbers above the top row denote the vertical profile positions for Fig. 5.

fireline and vertical distribution of C. For corresponding 1-min mean quantities, see Tables S1 and S2 and Movies S1–S3 in the online supplemental material. The spatiotemporal averaging is expressed as $\overline{\Phi}_{yt}$, where Φ is the variable name and "t" and "y" refer to averaging in time and the y direction, respectively.

Following the methodology employed in Kiefer et al. (2019, 2020), the particle residence time (RT) within a given radius or depth is used as a quantitative measure of particle dispersion in the horizontal and vertical dimensions, respectively: larger (smaller) RT corresponds to weaker (stronger) dispersion. RT was computed for each of the 300 000 particles released during the FLEXPART-WRF simulations. For each particle, horizontal RT (HRT) was computed within a distance of 50, 100, and 150 m from the center of the fire heat/$PM_{2.5}$ release zone (x direction only) and vertical RT (VRT) was computed within the forest canopy ($z \leq 18$ m). For consistency, the term "in canopy" is used to refer to the lowest 18 m of the atmosphere, regardless of the canopy profile shape or the height AGL where A_p diminishes to zero (Fig. 1). Finally, regarding directional references, the reader is reminded that the simulations in this study utilize a model domain with the x axis aligned west–east, a fireline extending south–north, and a westerly background wind; the terms "x axis," "x direction," "west/east," and "upstream/downstream," with the corresponding terms for the y axis, are used interchangeably.

3. Results and discussion

a. $PM_{2.5}$ concentration

Examination of the spatial distribution of $PM_{2.5}$ concentration begins with an analysis of 30-min mean $\overline{C}_{yt}$ vertical cross sections (Fig. 3), supported by tables of maximum $\overline{C}_{yt}$ at heights ≤ 18 m AGL (Table 1) and >18 m AGL (Table 2). For corresponding 1-min mean $\overline{C}_{yt}$ animations and supporting statistics, see Movie S1 and Tables S1 and S2, respectively. Figure 3 contains a 5 × 5 matrix of vertical cross sections with five A_p profiles, labeled A–E below the panels, and five fire sensible heat flux magnitudes, labeled 0–100 (kW m^{-2}) to the left of the panels. First, consider the hypothetical no-fire cases in the bottom row (labeled "0" in Fig. 3), included as a reference for comparisons with the cases with fire sensible heat flux. The reader is reminded that the no-fire simulations depict simulated $PM_{2.5}$ dispersion and concentration distribution in a hypothetical scenario in which the fire is weak enough that the uniform, steady net radiation flux intercepting the canopy top [section 2b(1)] is the dominant convective forcing for particle dispersion. In the absence of fire heat flux, $PM_{2.5}$ generally stays within the canopy, there is no preferred dispersion direction (west or east), and panel-maximum $\overline{C}_{yt}$ values increase as vertical canopy structure progresses from overstory-concentrated (shape A) to understory-concentrated (shape E). The lack of a preferred dispersion direction reflects the weak nature of $\overline{U}_{yt}$ in the forest canopy (30-min mean

TABLE 1. Maximum spatiotemporally averaged C [$\overline{C}_{yt}$ (y: y direction, t: 30-min)] in the near-fire area (denoted by dashed lines in Fig. 2), for $z \le 18$ m (μg m^{-3}). Units of heat flux are kilowatts per square meter. See Fig. 1 for plant area density profiles and Table S1 for corresponding 1-min mean C. As in Fig. 3, $\overline{C}_{yt}$ values are divided by 10^3.

	Canopy profile shape				
Heat flux	A	B	C	D	E
100	73.3	83.0	95.9	102.2	110.4
75	78.4	89.9	101.9	110.2	118.9
50	87.5	100.1	113.0	122.8	132.7
25	100.5	116.6	133.9	150.2	163.2
0	244.2	400.1	501.5	674.0	692.5

values are in the range of ±0.5 m s^{-1} in the bottom half of the layer; section 3b), the direct result of canopy drag. There is apparently a greater vertical dispersion of $PM_{2.5}$ out of the canopy with shapes B and C, possibly associated with individual large eddies in the convective boundary layer with time scales too long for the 30-min averaging procedure to completely eliminate. The greater penetration of large eddies into the canopy may be related to stronger canopy drag and weaker above-canopy $\overline{U}_{yt}$, with the more evenly distributed shape B and C plant area density profiles (section 3b). Nevertheless, above-canopy $\overline{C}_{yt}$ values with shapes B and C are less than 2% of the in-canopy maximum values (cf. Tables 1 and 2).

Proceeding to all rows in Fig. 3, two distinct changes from the bottom (no-fire) row are evident. First, the panel-maximum $\overline{C}_{yt}$ values are 58.8%–77.7% smaller in the 25 kW m^{-2} row compared to the no-fire row, indicating that the fire sensible heat source considerably increases particle dispersion compared to the background atmosphere. Further increases in fire sensible heat flux lead to further decreases in panel-maximum $\overline{C}_{yt}$, but the changes are smaller than seen between the no-fire and 25 kW m^{-2} rows. This relationship between fire sensible heat flux and $PM_{2.5}$ dispersion is supported by the ensemble-mean VRT and HRT values in Tables 3 and 4, respectively. The ensemble-mean VRT at or below 18 m AGL (HRT within 100 m of the release zone center) varies from 143.3–264.7 (194.6–316.7) s for the no-fire row to 48.3–82.6 (96.5–112.8) s for the 25 kW m^{-2} row to 33.3–54.8 (69.4–85.1) s for the 100 kW m^{-2} row; see

TABLE 2. Maximum spatiotemporally averaged C [$\overline{C}_{yt}$ (y: y direction, t: 30-min)] in the near-fire area (denoted by dashed lines in Fig. 2), for $z > 18$ m (μg m^{-3}). Units of heat flux are kilowatts per square meter. See Fig. 1 for plant area density profiles and Table S2 for corresponding 1-min mean C. As in Fig. 3, $\overline{C}_{yt}$ values are divided by 10^3.

	Canopy profile shape				
Heat flux	A	B	C	D	E
100	3.8	4.9	6.7	4.9	4.7
75	4.0	5.2	6.8	5.2	4.9
50	4.2	5.7	7.4	5.7	5.3
25	4.2	6.4	8.0	6.2	6.1
0	3.4	7.8	7.1	5.2	4.6

TABLE 3. Ensemble mean VRT inside the canopy ($z \le 18$ m) (s). Units of heat flux are kilowatts per square meter. See Fig. 1 for plant area density profiles and Table S3 for the number of particles in ensemble.

	Canopy profile shape				
Heat flux	A	B	C	D	E
100	33.3	35.4	40.2	48.0	54.8
75	35.8	37.5	42.7	51.3	59.8
50	39.5	42.5	47.8	58.0	67.2
25	48.3	52.8	58.2	73.4	82.6
0	143.3	185.8	213.8	261.7	264.7

Tables S3 and S4 for RT particle counts and Tables S5–S8 for additional HRT distances. The other distinct change is the presence of a distinct $PM_{2.5}$ plume in the cases with fire sensible heat flux. Unlike the no-fire panels, $\overline{C}_{yt}$ in the cases with a nonzero fire sensible heat flux is not necessarily maximized near the ground surface, as it is in the no-fire panels. That said, the overall distribution of $\overline{C}_{yt}$ exhibits little sensitivity to further increases in fire sensible heat flux. Note that the examination of the changes to $\overline{C}_{yt}$ as fire sensible heat flux is increased incrementally from 0 to 25 kW m^{-2} (i.e., in-between the bottom two rows in Fig. 3) is left to future work.

The consistent increasing trend in panel-maximum $\overline{C}_{yt}$ from shape A to shape E (proceeding from left to right in Fig. 3 and Table 1), first identified in the no-fire row analysis, indicates that as A_p progressively shifts from the overstory to the understory, the $PM_{2.5}$ dispersion decreases and near-fire concentration increases. This statement is supported by the ensemble-mean VRT values in Table 3, wherein the ensemble-mean VRT consistently increases from left to right, regardless of fire sensible heat flux magnitude. The relationship between the canopy profile shape and the ensemble-mean HRT is less straightforward, as the shortest (longest) HRT is found with the canopy profile shape A (C); this relationship is discussed further in section 3b. Regarding the $\overline{C}_{yt}$ distribution, shapes A, B, and C exhibit plumes tilted approximately 50% from vertical, with $PM_{2.5}$ spreading upward through the canopy into the overlying atmosphere, and shapes D and E exhibit plumes tilted about 80%–90% from vertical, with $PM_{2.5}$ largely remaining within the canopy. The tilt of the plume has implications for within-canopy $\overline{C}_{yt}$

TABLE 4. Ensemble mean HRT within 100 m of release zone center ($x \pm 100$ m) (s). Units of heat flux are kilowatts per square meter. See Fig. 1 for plant area density profiles, Table S4 for the number of particles in ensemble, and Tables S5–S8 for HRT values (and ensemble particle counts) for 50- and 150-m distances.

	Canopy profile shape				
Heat flux	A	B	C	D	E
100	69.4	76.0	85.1	77.1	76.5
75	74.1	80.1	89.1	81.1	81.1
50	81.7	88.9	97.3	87.2	88.1
25	96.5	104.6	112.8	102.5	103.6
0	194.6	270.5	288.7	316.7	293.4

at distances of 100 m or more to the east (downstream) of the heat source/particle release zone center. At those distances, in-canopy $\overline{C}_{yt}$ is 70%–80% lower with shape A than with shape E (for $\overline{C}_{yt}$ farther downstream, see Fig. S1). Broadly speaking, this pattern becomes more pronounced as the fire sensible heat flux increases. However, caution is recommended when examining in-canopy $\overline{C}_{yt}$ away from the release zone, as particle deposition on vegetation and ground surfaces is not considered in this study.

Lastly, note that there is a sharp western edge to the $PM_{2.5}$ plume above or just upwind of the fire heat source, with $\overline{C}_{yt}$ values west of this edge less than 1% of the cross-sectional maximum (cf. color-fill threshold in Fig. 3 to cross-sectional maximum depicted in the upper-left corner of each panel). The notable exception is the lowest few levels of the canopy atmosphere where weak flow allows particles to drift westward, and nonnegligible $\overline{C}_{yt}$ values extend 50 m or more upstream (i.e., west) of the release zone. Before proceeding, a few words are in order regarding the potential impact of the 2.5 m s^{-1} background wind speed (reduced through drag to less than 1 m s^{-1} in the lower canopy) on the broader applicability of our results. The relationships between $PM_{2.5}$ concentration distribution, canopy profile shape, and fire sensible heat flux identified in this study may not apply to cases with stronger background wind speeds and/or winds that exhibit considerable vertical variability. The reader is urged to keep this important limitation in mind when considering the broader applicability of study results.

To further explore the distribution of $\overline{C}_{yt}$, we next consider horizontal (Fig. 4) and vertical (Fig. 5) profiles extracted from the 30-min mean $\overline{C}_{yt}$ cross sections in Fig. 3 (near-fire area) and Fig. S1 (full domain). Given the orders of magnitude differences in $\overline{C}_{yt}$ across the near-fire area and the broader model domain, semilog axes are utilized (Fig. 4: log y axis; Fig. 5: log x axis). Considering horizontal profiles of 0–2 m AGL $\overline{C}_{yt}$ first (Fig. 4), values are shown to vary five or more orders of magnitude across the entire west–east domain dimension (Fig. 4a) and two or more orders of magnitude across the near-fire area alone (Fig. 4b). Focusing specifically on the near-fire area (Fig. 4b), it is apparent that the application of the fire sensible heat source yields a more rapid decline in $\overline{C}_{yt}$ with the horizontal distance from the release zone, compared to the no-fire case. Using the shape E cases as a collective example, the slope in the semilog plot is approximately one order of magnitude per 50-m distance downstream (i.e., eastward) without the fire sensible heat source but about one and one-half orders of magnitude per 50-m distance with the fire sensible heat source. Generally speaking, the $\overline{C}_{yt}$ horizontal gradient increases in magnitude with increasing fire sensible heat flux.

Finally, we consider the five vertical profiles denoted by vertical dashed lines in Fig. 3, one upstream (i.e., west) of the release zone (P1), one centered on the release zone (P2), and three downstream (i.e., east) of the release zone (P3–P5) (Fig. 5). Over and upstream (west) of the release zone (profiles P1–P2), one finds decreasing $\overline{C}_{yt}$ with height, regardless of the canopy profile shape or fire sensible heat flux magnitude. Such a result is not unexpected, given the 0–2 m AGL particle release layer in FLEXPART-WRF. However, the $\overline{C}_{yt}$ vertical distribution at profiles P1 and P2 does exhibit some sensitivity to the control

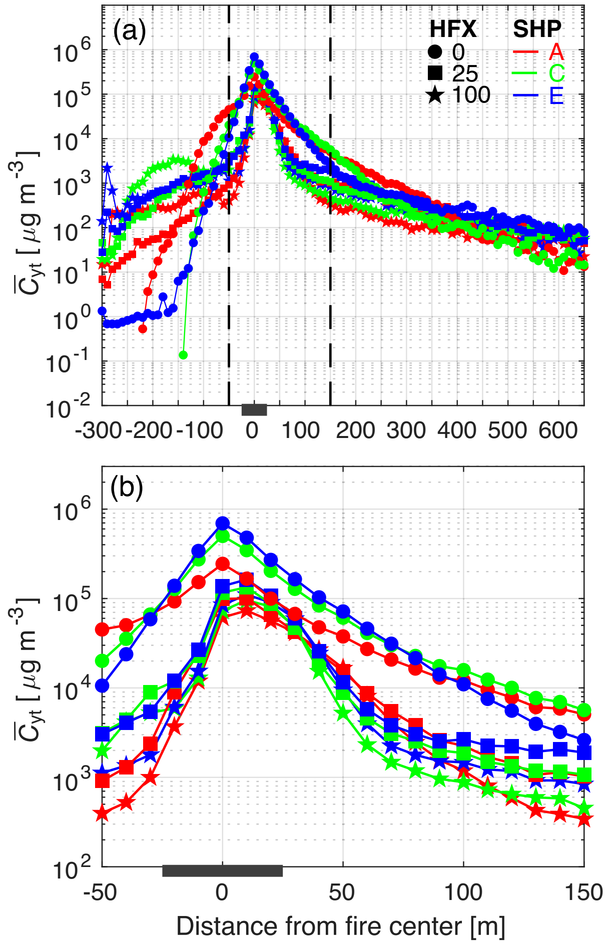

FIG. 4. Horizontal profiles of spatiotemporally averaged C [$\overline{C}_{yt}$ (y: y direction, t: 30-min)] in layer 0–2 m AGL, across the (a) full domain and (b) near-fire area, displayed with linear x axis and log y axis. See legend in (a) for the explanation of symbols (fire sensible heat flux: "HFX") and colors (canopy profile shape: "SHP"); for clarity, two canopy profile shapes (B and D) and two fire sensible heat fluxes (50 and 75 kW m^{-2}) are omitted.

parameters. At profile P1, for the cases with nonzero fire sensible heat flux, the vertical gradient within the canopy increases in magnitude as the vegetation profile becomes increasingly understory-concentrated (i.e., shape A → shape E); however, for the no-fire reference cases, the vertical gradient is largely insensitive to changes to the canopy profile shape. For cases with the same canopy profile shape, increasing the fire sensible heat flux from 25 to 100 kW m^{-2} yields progressively weaker vertical gradients of $\overline{C}_{yt}$ (a reflection of stronger vertical mixing with stronger sensible heat sources). At profile P2, directly above the release zone, a two-layer "hockey stick" $\overline{C}_{yt}$ profile shape is found in all cases, with the strongest vertical gradient across the lowest 2–3 grid levels and a weaker gradient above. Unlike at profile P1, a consistent relationship between the $\overline{C}_{yt}$ vertical distribution and either canopy profile shape or fire sensible heat flux magnitude is difficult to discern. Although the $\overline{C}_{yt}$ vertical distribution is sensitive to these parameters, a readily identifiable pattern is lacking.

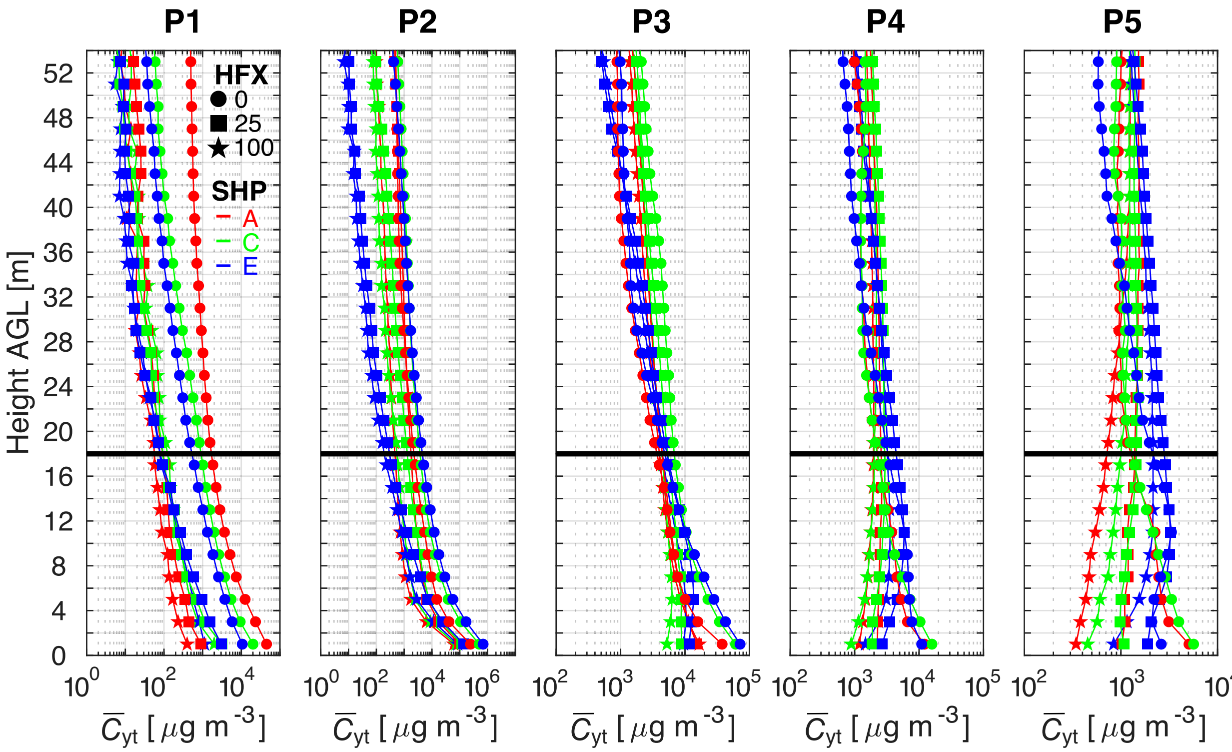

FIG. 5. Vertical profiles of spatiotemporally averaged C [$\overline{C}_{yt}$ (y: y direction, t: 30-min)] at five profile points depicted in Fig. 3, displayed with log x axis and linear y axis. See legend in the first panel for the explanation of symbols (HFX) and colors (SHP); for clarity, two canopy profile shapes (B and D) and two fire sensible heat fluxes (50 and 75 kW m^{-2}) are omitted.

At profile positions increasingly farther downstream (i.e., east) of the release zone (profiles P3–P5), the maximum values of the $\overline{C}_{yt}$ shift from the surface to a position midcanopy or higher, in the cases with fire sensible heat flux, but remain anchored at the surface in the no-fire cases. At profiles P4 and P5, with the exception of the no-fire reference cases, a midcanopy $\overline{C}_{yt}$ maximum is found with understory-concentrated canopy profile shapes D and E and an above-canopy $\overline{C}_{yt}$ maximum is found with the other canopy profile shapes (shapes B and D not shown; recall from section 2c that "in canopy" refers to the lowest 18 m of the atmosphere). In other words, there is a tendency in the FLEXPART-WRF simulations for $\overline{C}_{yt}$ downstream (i.e., east) of the release zone to be maximized closer to the surface with understory-concentrated canopy profiles than with overstory-concentrated canopy profiles.

b. *Meteorological variables*

We now proceed to the analysis of the ARPS-CANOPY meteorological variables directly driving the $PM_{2.5}$ dispersion in FLEXPART-WRF: U, W, and E^S; recall from section 2c that V is used internally by FLEXPART-WRF but is not explicitly analyzed because of the study focus on the vertical and cross-fire distribution of $PM_{2.5}$ concentration (hence the y axis averaging of C). In addition to the ARPS-CANOPY variables ingested into FLEXPART-WRF, E^R [derived from instantaneous U, V, and W; Eq. (1)] is also analyzed. The purpose of this analysis is to gain insight into the dispersion processes yielding the $\overline{C}_{yt}$ distribution documented in Figs. 3–5: mean transport and turbulent diffusion (achieved through a combination of grid-resolved and SGS turbulent eddies). Due to the difficulty in partitioning total dispersion into mean transport, grid-resolved turbulent diffusion, and SGS turbulent diffusion, this analysis is generally qualitative in nature.

Before proceeding to the analysis, it is important to clarify that the vertical cross sections of the 30-min mean $\overline{U}_{yt}$ and $\overline{W}_{yt}$, $\overline{E^R}_{yt}$, and $\overline{E^S}_{yt}$ communicate information about mean transport, grid-resolved turbulent diffusion, and SGS turbulent diffusion, respectively. In addition to vertical cross sections of $\overline{E^R}_{yt}$, the grid-resolved turbulent diffusion is discussed in the context of the corresponding animations of 1-min mean $\overline{C}_{yt}$, $\overline{U}_{yt}$, and $\overline{W}_{yt}$ included in Movies S1–S3. The reader is reminded that the ARPS-CANOPY simulations driving the FLEXPART-WRF particle dispersion were initialized with a 2.5 m s^{-1} background wind speed (reduced via drag to 1 m s^{-1} or less in the lower canopy).

Analysis begins with vertical cross sections of 30-min mean $\overline{U}_{yt}$ (Fig. 6) and $\overline{W}_{yt}$ (Fig. 7). As in the earlier discussion of $\overline{C}_{yt}$ (Fig. 3), we start with the no-fire cases in the bottom row of each figure. In the absence of fire sensible heat flux, $\overline{U}_{yt}$ near and above canopy top (18 m AGL) is 1–2.5 m s^{-1} (diminished via canopy drag from the 2.5 m s^{-1} initial state), and below canopy top is -0.1–2 m s^{-1}. The negative $\overline{U}_{yt}$ below canopy top is limited to the lowest model level in the case with canopy profile shape A and appears to be associated

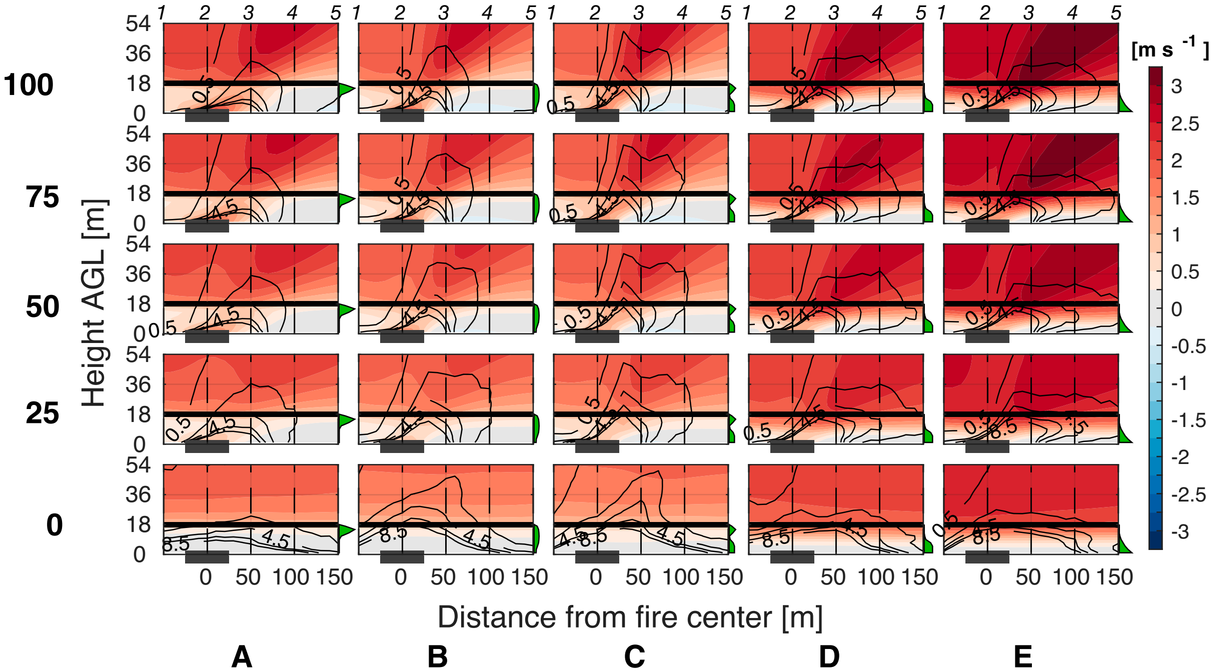

FIG. 6. Vertical cross sections of spatiotemporally averaged U [$\overline{U}_{yt}$ (y: y direction, t: 30-min); shaded] in the near-fire area (denoted by dashed lines in Fig. 2), with spatiotemporally averaged C overlaid [$\overline{C}_{yt}$ (y: y direction, t: 30-min); contoured], arranged in a 5 × 5 matrix with vertical canopy structure varying between panels along the x axis (canopy profiles A–E) and fire heat flux magnitude varying between panels along the y axis (kW m^{-2}). The $\overline{C}_{yt}$ is contoured from 500 to 8500 μg m^{-3}, with a 200 μg m^{-3} interval; to conserve space, $\overline{C}_{yt}$ values are divided by 10^3. The horizontal line at 18 m denotes the canopy top, the thick black bar at the bottom of the panel depicts the fireline, and the green-filled shape to the right of the panel depicts the plant area density profile. Numbers above the top row denote the vertical profile positions for Fig. 5.

with transient turbulent eddies not completely eliminated by the 30-min averaging procedure (see 1-min mean $\overline{U}_{yt}$ and $\overline{W}_{yt}$ in Movies S2 and S3). Overall, the weakest (strongest) above-canopy $\overline{U}_{yt}$ is found with shapes B and C (D and E); the relatively weak $\overline{U}_{yt}$ with shapes B and C is likely a reflection of stronger overall drag associated with the more evenly distributed nature of A_p compared to the other canopy profile shapes (broadly consistent with Dupont and Brunet 2008). As expected in the convective boundary layer, $\overline{W}_{yt}$ is smaller than ±0.1 m s^{-1} (Stull 1988). The overall weak nature of mean transport implied by within-canopy $\overline{U}_{yt}$ and $\overline{W}_{yt}$ (Figs. 6 and 7), combined with the steady $PM_{2.5}$ particle release rate, contributes to the large $\overline{C}_{yt}$ in the no-fire cases (Figs. 3–5, Table 1).

As noted by Kiefer et al. (2018) and as seen in the bottom two rows of Figs. 6 and 7, the introduction of the fire sensible heat flux drastically alters $\overline{U}_{yt}$ and $\overline{W}_{yt}$. With the fire sensible heat flux, an eastward-tilted updraft and flanking downdraft are anchored inside the canopy (Fig. 7), with corresponding near-surface westerly and easterly inflow and above-canopy westerly outflow (Fig. 6). This overall pattern remains unchanged as fire sensible heat flux increases from 25 to 100 kW m^{-2}, although the magnitudes of $\overline{U}_{yt}$ and $\overline{W}_{yt}$ steadily increase. Notably, the depth of the easterly inflow (to the east of the fire sensible heat source in Fig. 6) decreases as A_p progressively shifts from the overstory (shape A) to the understory (shape E). Comparing the patterns of $\overline{C}_{yt}$ with those of $\overline{U}_{yt}$ and $\overline{W}_{yt}$ (i.e., contours and shading in Figs. 6 and 7), it appears that mean transport via the tilted updraft is a primary dispersion mechanism with shapes A–C but not shapes D and E. Recall that quasi-steady fire-induced phenomenon such as the updraft is classified in this study as part of the mean flow, as in Kiefer et al. (2018). The $\overline{C}_{yt}$ pattern in the cases with shapes D and E appears to closely align with the layer of strongest vertical $\overline{U}_{yt}$ shear in Fig. 6. The role of vertical wind shear in the dispersion of $PM_{2.5}$ will be discussed shortly in the context of resolved and SGS turbulent diffusion.

Proceeding from the analysis of mean transport to the analysis of grid-resolved and SGS turbulent diffusion, $\overline{E^R}_{yt}$ and $\overline{E^S}_{yt}$ are shown in Figs. 8 and 9, respectively. Beginning with the bottom row in Fig. 8, $\overline{E^R}_{yt}$ magnitudes in the absence of fire sensible heat flux vary from as small as 0.125 m^2 s^{-2} or less in the lower canopy with shapes D and E, to as large as about 1 m^2 s^{-2} above the canopy with shapes C and D. The presence of near-surface $\overline{E^R}_{yt}$ on the order of 0.5 m^2 s^{-2} with canopy shape A suggests a nonnegligible contribution of grid-resolved turbulent diffusion to particle dispersion in the sparsely vegetated lower canopy (where canopy drag is minimized, relative to the upper canopy); the relatively small panel-maximum $\overline{C}_{yt}$ seen in Fig. 3 (bottom-left panel) is consistent with enhanced turbulent diffusion in the lower canopy. Taking together the no-fire $\overline{E^R}_{yt}$ and $\overline{E^S}_{yt}$ values in Figs. 8 and 9, respectively, the above-canopy $\overline{E^T}_{yt}$ values (∼0.5–1 m^2 s^{-2},

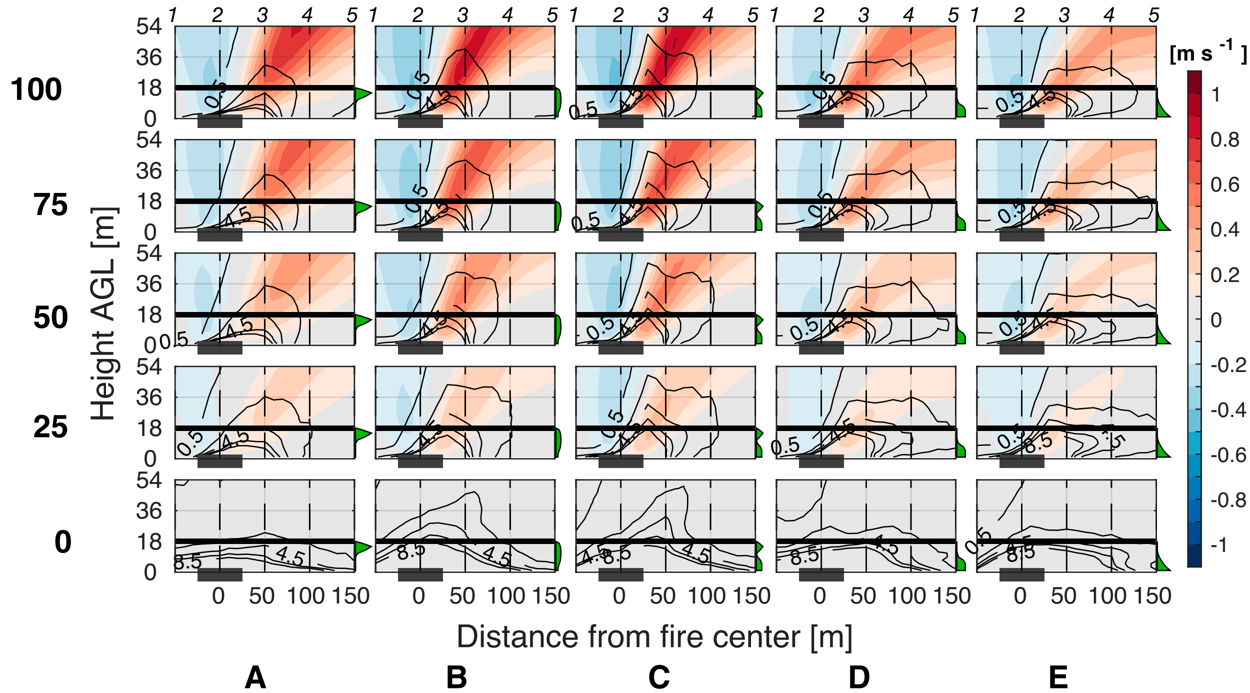

FIG. 7. As in Fig. 6, but for $\overline{W}_{yt}$.

not shown) are suggestive of a weakly turbulent background atmosphere (~2–3 m^2 s^{-2} is indicative of a substantially turbulent lower PBL; Stull 1988).

Introduction of the 25 kW m^{-2} fire sensible heat flux yields $\overline{E^R}_{yt}$ values as large as 1–1.5 m^2 s^{-2}, with the canopy shape A and B cases exhibiting two distinct maxima (near-surface and above-canopy) and the other three cases exhibiting a single maximum near or above the canopy top. Further increases in sensible heat flux from 25 to 100 kW m^{-2} have a minimal impact on the $\overline{E^R}_{yt}$ pattern, with $\overline{E^R}_{yt}$ magnitude increasing to about 2–3 m^2 s^{-2} in the 100 kW m^{-2} row, largest with canopy shape C. It is worth noting the overall pattern similarity between $\overline{U}_{yt}$ (Fig. 6) and $\overline{E^R}_{yt}$ (Fig. 8), with the above-canopy $\overline{E^R}_{yt}$ maximum generally positioned downstream (east) of and groundward of the corresponding $\overline{U}_{yt}$ maximum. The approximate collocation of the above-canopy $\overline{E^R}_{yt}$ maxima and the layer of strongest vertical $\overline{U}_{yt}$ shear suggests the important role of shear production in the downscale energy transfer from the mean flow to turbulent eddies (Stull 1988). The presence of a near-surface $\overline{E^R}_{yt}$ maximum near and immediately downstream of the fire sensible heat source in cases with canopy shapes A and B indicates the role of buoyancy production in the generation of enhanced $\overline{E^R}_{yt}$; see $\overline{T}_{yt}$ in Fig. S2. An $\overline{E^R}_{yt}$ budget analysis is beyond the scope of this study; however, analysis of E^R production terms in previous ARPS-CANOPY simulations of low-intensity fires (Kiefer et al. 2014, 2015) supports the argument that both buoyancy and shear production are important sources of $\overline{E^R}_{yt}$ in this study. However, the absence of a near-surface $\overline{E^R}_{yt}$ maximum in the other three cases (Fig. 8) points to the strong damping role of canopy drag on the near-surface E^R production in the presence of understory A_p maxima. Finally, the finding from section 3a that HRT is smallest (largest) with canopy profile shape A (C) (Table 4) is explained by the presence of near-surface $\overline{U}_{yt}$ and $\overline{E^R}_{yt}$ maxima with canopy profile shape A (cf. Figs. 6 and 8), yielding a relatively strong horizontal dispersion, and the presence of the strongest $\overline{W}_{yt}$ (and thus more vertical particle trajectories) with canopy profile shape C (Fig. 7), yielding a relatively weak horizontal dispersion.

For further analysis of grid-resolved turbulent diffusion, the reader is invited to review animations of 1-min mean $\overline{C}_{yt}$, $\overline{U}_{yt}$ and $\overline{W}_{yt}$ in Movies S1–S3. In Movies S1–S3, large eddies manifest in the near-fire area as alternating periods of stronger and weaker 1-min mean $\overline{U}_{yt}$ (Movie S2) and $\overline{W}_{yt}$ (Movie S3), enhanced and suppressed $PM_{2.5}$ dispersion, and lower and higher 1-min mean $\overline{C}_{yt}$ (Movie S1). In the no-fire cases, only transient eddies are present, whereas in the cases with fire sensible heat flux, transient features are superimposed on a pulsating fire-induced circulation (e.g., see fluctuating updraft). It is worth noting that Heilman et al. (2021) found evidence of periodicity in fire-induced coherent structures within and near the fire environment during a low-intensity prescribed fire in the New Jersey Pine Barrens; further examination of this phenomenon is left to future work. Finally, the juxtaposition of the area of fire-induced $\overline{E^R}_{yt}$ and the $\overline{C}_{yt}$ plume (Fig. 8) indicates that grid-resolved turbulent eddies are playing an important role in the dispersion of $PM_{2.5}$ particles upward through the canopy and downstream (east) of the surface sensible heat source.

Proceeding to $\overline{E^S}_{yt}$ (Fig. 9), it is evident that in the absence of the fire sensible heat source, E^S is small ($\overline{E^S}_{yt} \lesssim 0.05$ m^2 s^{-2}). The only $\overline{E^S}_{yt}$ values exceeding the 0.05 m^2 s^{-2} color-fill

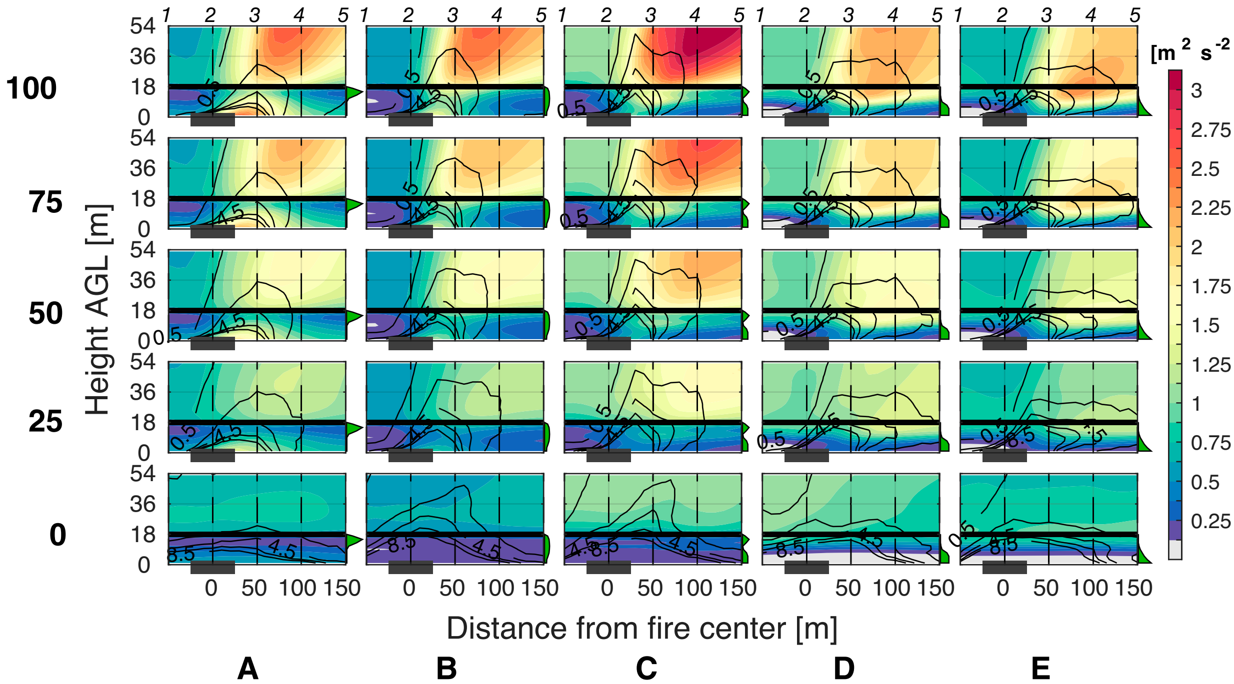

FIG. 8. As in Fig. 6, but for $\overline{E^R}_{yt}$.

threshold in the bottom row of Fig. 9 occur in the simulations with canopy shapes D and E; note the correspondence between the layer of strongest vertical $\overline{U}_{yt}$ shear in Fig. 6 and the layer with $\overline{E^S}_{yt}$ exceeding 0.05 m^2 s^{-2} in Fig. 9 (near 9 m AGL). Introduction of the fire sensible heat source yields a $\overline{E^S}_{yt}$ maximum 1–2 grid points above the fire-induced $\overline{T}_{yt}$ maximum for all canopy profile shapes (cf. Fig. 9 and Fig. S2). $\overline{E^S}_{yt}$ is also enhanced near 18 m AGL (shapes A–C) and 9 m AGL (shapes D–E), corresponding approximately to the heights of maximum vertical $\overline{U}_{yt}$ shear in Fig. 6. The overall $\overline{E^S}_{yt}$ pattern

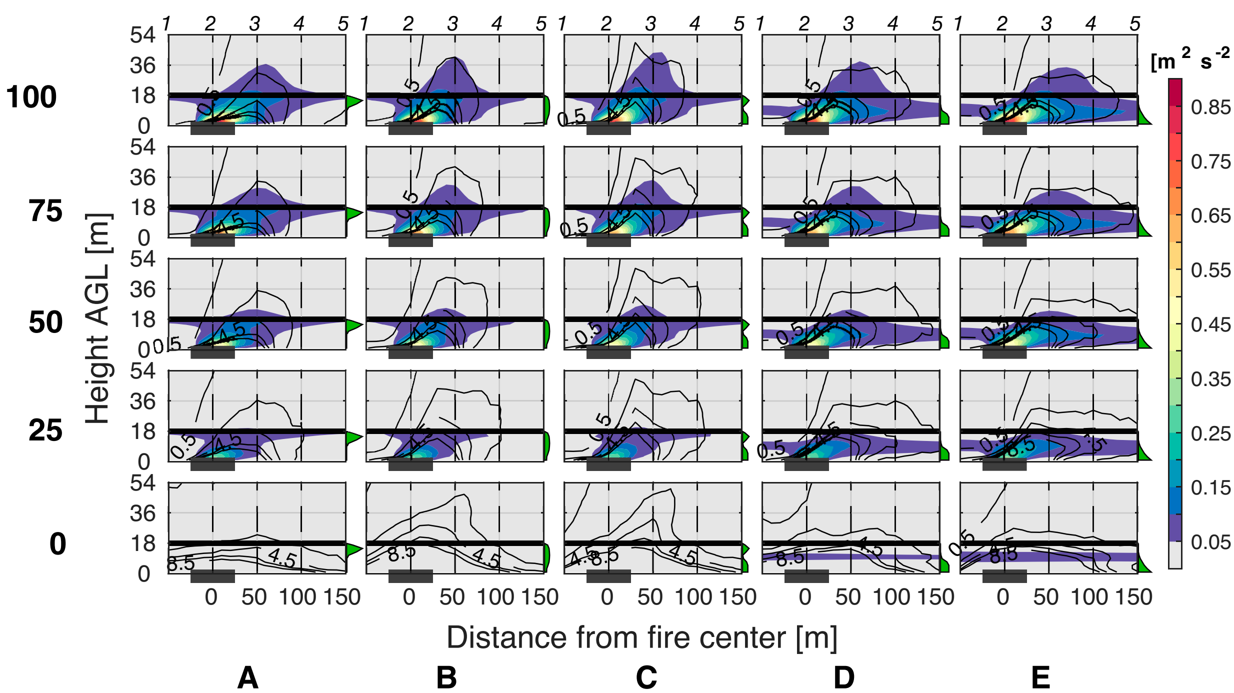

FIG. 9. As in Fig. 6, but for $\overline{E^S}_{yt}$.

is unchanged as fire sensible heat flux is increased, with the magnitude of $\overline{E^S}_{yt}$ increasing to a maximum of ~0.8 m^2 s^{-2} in the case with the shape E canopy profile and 100 kW m^{-2} fire sensible heat flux. Close comparison of the magnitudes of $\overline{E^R}_{yt}$ and $\overline{E^S}_{yt}$ (cf. Figs. 8 and 9) leads to the conclusion that although the largest $\overline{E^S}_{yt}$ value is about four times smaller than the largest $\overline{E^R}_{yt}$ value, the ratio of $\overline{E^S}_{yt}$ to $\overline{E^T}_{yt}$ is as large as 0.85 immediately above the fireline and generally exceeds 0.1 in the areas of Fig. 9, where $\overline{E^S}_{yt}$ exceeds the 0.1 m^2 s^{-2} color-fill threshold. In the cases with canopy profile shapes D and E, FLEXPART-WRF appears to partition the E^S-derived random wind components such that the horizontal SGS turbulent diffusion dominates midcanopy (~9 m AGL). It is important to keep in mind that the E^S variable in ARPS-CANOPY is computed from a prognostic equation that includes canopy source and sink terms (Xue et al. 2000; Kiefer et al. 2013). Finally, the collocation of the $PM_{2.5}$ plume indicated by the $\overline{C}_{yt}$ contours and the areas of fire-enhanced $\overline{E^R}_{yt}$ (Fig. 8) and $\overline{E^S}_{yt}$ (Fig. 9) suggests that grid-resolved (SGS) turbulent diffusion is playing an important role in the dispersion of $PM_{2.5}$, mainly outside (inside) of the canopy.

4. Summary and conclusions

In this study, a Lagrangian particle dispersion model (FLEXPART-WRF) was used to address two research questions concerning the distribution of smoke from low-intensity prescribed fires in forested environments. First, what is the relationship between near-fire smoke concentration distribution and (i) vertical canopy structure and (ii) fire heat source strength? Second, what roles do mean transport and turbulent diffusion play in shaping the near-fire smoke concentration distribution? To help answer these questions, FLEXPART-WRF was used to simulate $PM_{2.5}$ dispersion from low-intensity surface fires using the meteorological output from a full-physics atmospheric model with a forest canopy submodel (ARPS-CANOPY). Simulations were run with 25 combinations of A_p profiles and fire sensible heat flux magnitudes. Among the 25 cases, a set of five no-fire simulations served as a reference for the 20 simulations with fire sensible heat flux. The no-fire simulations depicted $PM_{2.5}$ dispersion and concentration distribution in a hypothetical very-weak-fire scenario in which the uniform, steady net radiation flux intercepting the canopy top [section 2b(1)] was the dominant convective forcing for particle dispersion. The analysis focused on the near-fire area and included vertical cross sections and profiles of $PM_{2.5}$ concentration, vertical cross sections of the ARPS-CANOPY variables driving $PM_{2.5}$ dispersion, and summary statistics relating $PM_{2.5}$ concentration distribution, $PM_{2.5}$ dispersion, vertical canopy structure, and fire heat source magnitude.

Results showed that $PM_{2.5}$ concentration distribution in the near-fire area is primarily controlled by vertical canopy structure, with fire heat source strength primarily controlling the $PM_{2.5}$ concentration magnitude (research question 1). In the absence of fire sensible heat flux, there was no preferred dispersion direction (west or east), a consequence of light mean wind speeds within the forest canopy, and surface $PM_{2.5}$ concentration values generally increased as vertical canopy structure progressed from overstory-concentrated (shape A) to understory-concentrated (shape E). With the fire sensible heat source applied, a distinct $PM_{2.5}$ plume was found with all canopy profile shapes, anchored in the release zone. As fire sensible heat flux increased, $PM_{2.5}$ dispersion increased and surface $PM_{2.5}$ concentration decreased, but the overall $PM_{2.5}$ concentration pattern remained unchanged. However, the overall $PM_{2.5}$ concentration distribution within and above the canopy showed marked sensitivity to the forest canopy profile shape: shapes A, B, and C exhibited plumes tilted downstream approximately 50% from vertical, with $PM_{2.5}$ spreading upward through the canopy into the overlying atmosphere, whereas shapes D and E exhibited plumes tilted downstream approximately 80%–90% from vertical, with $PM_{2.5}$ remaining largely inside the canopy.

Analysis of the underlying ARPS-CANOPY variables driving FLEXPART-WRF dispersion helped elucidate the relative roles of mean transport and turbulent diffusion, both grid-resolved and SGS (research question 2). Of particular note was the role that the quasi-steady fire-induced circulation (i.e., updraft, surface inflow, and above-canopy outflow) played in driving mean transport, especially in the cases with overstory-concentrated A_p profiles (shapes A and B), and the role that SGS TKE played in driving horizontal SGS turbulent diffusion inside the forest canopy, especially in the simulations with understory-concentrated A_p profiles (shapes D and E). However, the reader is reminded that there is currently no consensus in the fire weather research community as to whether fire-induced quasi-steady phenomena should be classified as coherent turbulent structures or as fire-induced modifications to the ambient mean flow.

Taken as a whole, the study findings suggest that the vertical distribution of forest canopy vegetation (as measured by the vertical distribution of A_p) and fire heat source strength (as measured by fire sensible heat flux magnitude) are important factors that influence the horizontal and vertical distributions of $PM_{2.5}$ concentration in the near-fire area [i.e., the area of the overlying atmosphere within about 50–150 m (~3–10 canopy heights) of a low-intensity surface fire]. As noted in section 1, knowledge of the distribution of $PM_{2.5}$ concentration in the near-fire area, particularly the tendency of smoke to either remain within the forest canopy or move out of the canopy, may help inform studies of smoke concentration distribution across deeper layers of the atmosphere and the associated local- to regional-scale dispersion. To that end, possible study applications include 1) utilizing the 25-case matrix as a reference smoke dataset for validating smoke output from quick-response fire–atmosphere modeling tools that lack a full-physics atmospheric model [e.g., QUIC-fire (Linn et al. 2020)]; 2) developing smoke dispersion parameterizations for inclusion in models and modeling frameworks that do not explicitly resolve flows within forest canopies [e.g., High-Resolution Rapid Refresh (HRRR)-smoke (Ahmadov et al. 2017, 2021); BlueSky (Larkin et al. 2009)]; and 3) transforming model results into actionable guidance for fire managers seeking to tailor their prescribed burn plans to maximize smoke dispersion from surface fires.

Despite the progress documented herein, much work remains. Study limitations include the use of a static fire-induced sensible heat source within a horizontally homogeneous forest canopy, the omission of fire-induced latent heat fluxes, the utilization of a single 2.5 m s^{-1} background wind speed, and the use of 10-m-wide grid cells that prohibit the simulation of finer-scale turbulent phenomena such as fireline vortices. The reader is reminded that the smoke–canopy–fire relationships examined in this study may be sensitive to the magnitude and vertical variability of the background wind. Inspired by the recent USFS smoke science assessment (Liu et al. 2022), planned future work includes performing additional FLEXPART-WRF simulations driven by output from 1) ARPS-CANOPY simulations with (i) forest gaps, (ii) multiple fire heat zones, (iii) time-varying heat sources, (iv) different background wind profiles, and (v) 1-m grid spacing (to evaluate the sensitivity of results to the SGS turbulence parameterization); and 2) simulations conducted with ARPS-CANOPY-Discrete Event System Specification Fire model (ARPS-CANOPY-DEVS-FIRE), a coupled fire–atmosphere modeling system based on ARPS-DEVS-FIRE (Dahl et al. 2015) that is currently under development.

Acknowledgments. Support for this research was provided by the USDA Forest Service via Research Joint Venture Agreement 20-JV-11242306-070 and by the USDA National Institute of Food and Agriculture Hatch Project MICL02754. The color maps used in Figs. 3 and 6–9, Figs. S1 and S2, and Movies S1–S3 were developed by Cynthia Brewer at the Pennsylvania State University (http://colorbrewer2.org/). Finally, comments and suggestions from three anonymous reviewers were helpful in revising the manuscript and are greatly appreciated.

Data availability statement. Datasets and software code associated with this study have been uploaded to the Harvard Dataverse (https://doi.org/10.7910/DVN/BB16X4). Data are available under the terms of the Creative Commons Zero "No rights reserved" data waiver (CC0 1.0 Public domain dedication).

REFERENCES

Ahmadov, R., and Coauthors, 2017: A high-resolution coupled meteorology-smoke modeling system HRRR-smoke to simulate air quality over the CONUS domain in real time. *Geophysical Research Abstracts*, Vol. 19, Abstract 10841, https://meetingorganizer.copernicus.org/EGU2017/EGU2017-10841.pdf.

——, E. James, G. Grell, C. Alexander, and S. McKeen, 2021: Operational implementation of the smoke forecasting capability in the RAP/HRRR numerical weather prediction system. *2021 EGU General Assembly*, Online, European Geosciences Union, EGU21-14268, https://doi.org/10.5194/egusphere-egu21-14268.

Bahlali, M. L., C. Henry, and B. Carissimo, 2020: On the well-mixed condition and consistency issues in hybrid Eulerian/Lagrangian stochastic models of dispersion. *Bound.-Layer Meteor.*, **174**, 275–296, https://doi.org/10.1007/s10546-019-00486-9.

Brioude, J., and Coauthors, 2013: The Lagrangian particle dispersion model FLEXPART-WRF version 3.1. *Geosci. Model Dev.*, **6**, 1889–1904, https://doi.org/10.5194/gmd-6-1889-2013.

Charney, J. J., and Coauthors, 2019: Assessing forest canopy impacts on smoke concentrations using a coupled numerical model. *Atmosphere*, **10**, 273, https://doi.org/10.3390/atmos10050273.

Chou, M.-D., 1990: Parameterization for the absorption of solar radiation by O_2 and CO_2 with application to climate studies. *J. Climate*, **3**, 209–217, https://doi.org/10.1175/1520-0442(1990)003<0209:PFTAOS>2.0.CO;2.

——, 1992: A solar radiation model for use in climate studies. *J. Atmos. Sci.*, **49**, 762–772, https://doi.org/10.1175/1520-0469(1992)049<0762:ASRMFU>2.0.CO;2.

——, and M. J. Suarez, 1994: An efficient thermal infrared radiation parameterization for use in general circulation models. NASA Tech. Memo. 104606/Vol. 3, 98 pp.

Clements, C. B., and Coauthors, 2007: Observing the dynamics of wildland grass fires: FireFlux–A field validation experiment. *Bull. Amer. Meteor. Soc.*, **88**, 1369–1382, https://doi.org/10.1175/BAMS-88-9-1369.

Cornwell, G. C., H. Xiao, L. K. Berg, and S. M. Burrows, 2021: Simulated dust transport in the convective boundary layer. *J. Geophys. Res. Atmos.*, **126**, e2020JD033429, https://doi.org/10.1029/2020JD033429.

Dahl, N., H. Xue, X. Hu, and M. Xue, 2015: Coupled fire–atmosphere modeling of wildland fire spread using DEVS-FIRE and ARPS. *Nat. Hazards*, **77**, 1013–1035, https://doi.org/10.1007/s11069-015-1640-y.

Deardorff, J. W., 1980: Stratocumulus-capped mixed layers derived from a three-dimensional model. *Bound.-Layer Meteor.*, **18**, 495–527, https://doi.org/10.1007/BF00119502.

Dupont, S., and Y. Brunet, 2008: Influence of foliar density profile on canopy flow: A large-eddy simulation study. *Agric. For. Meteor.*, **148**, 976–990, https://doi.org/10.1016/j.agrformet.2008.01.014.

Engebretson, J. M., T. E. Hall, J. J. Blades, C. S. Olsen, E. Toman, and S. S. Frederick, 2016: Characterizing public tolerance of smoke from wildland fires in communities across the United States. *J. For.*, **114**, 601–609, https://doi.org/10.5849/jof.14-142.

Hanna, S. R., 1982: Applications in air pollution modeling. *Atmospheric Turbulence and Air Pollution Modeling*, F. T. M. Nieuwstadt, and H. D. van Dop, Eds., Reidel Publishing Company, 275–310.

Heilman, W. E., C. B. Clements, D. Seto, X. Bian, K. L. Clark, N. S. Skowronski, and J. L. Hom, 2015: Observations of fire-induced turbulence regimes during low-intensity wildland fires in forested environments: Implications for smoke dispersion. *Atmos. Sci. Lett.*, **16**, 453–460, https://doi.org/10.1002/asl.581.

——, K. L. Clark, X. Bian, J. J. Charney, S. Zhong, N. S. Skowronski, M. R. Gallagher, and M. Patterson, 2021: Turbulent momentum flux behavior above a fire front in an open-canopied forest. *Atmosphere*, **12**, 956, https://doi.org/10.3390/atmos12080956.

Hiers, J. K., R. Ottmar, B. W. Butler, C. Clements, R. Vihnanek, M. B. Dickinson, and J. O'Brien, 2009: An overview of the prescribed Fire Combustion and Atmospheric Dynamics Research Experiment (Rx-CADRE). *Fourth Int. Fire Ecology and Management Congress: Fire as a Global Process*, Savannah, GA, Association for Fire Ecology.

——, and Coauthors, 2020: Prescribed fire science: The case for a refined research agenda. *Fire Ecol.*, **16**, 11, https://doi.org/10.1186/s42408-020-0070-8.

Jaffe, D. A., S. M. O'Neill, N. K. Larkin, A. L. Holder, D. L. Peterson, J. E. Halofsky, and A. G. Rappold, 2020: Wildfire and prescribed burning impacts on air quality in the United States.

J. Air Waste Manage. Assoc., **70**, 583–615, https://doi.org/10.1080/10962247.2020.1749731.

Kiefer, M. T., S. Zhong, W. E. Heilman, J. J. Charney, and X. Bian, 2013: Evaluation of an ARPS-based canopy flow modeling system for use in future operational smoke prediction efforts. *J. Geophys. Res. Atmos.*, **118**, 6175–6188, https://doi.org/10.1002/jgrd.50491.

——, and Coauthors, 2014: Multiscale simulation of a prescribed fire event in the New Jersey Pine Barrens using ARPS-CANOPY. *J. Appl. Meteor. Climatol.*, **53**, 793–812, https://doi.org/10.1175/JAMC-D-13-0131.1.

——, W. E. Heilman, S. Zhong, J. J. Charney, and X. Bian, 2015: Mean and turbulent flow downstream of a low-intensity fire: Influence of canopy and background atmospheric conditions. *J. Appl. Meteor. Climatol.*, **54**, 42–57, https://doi.org/10.1175/JAMC-D-14-0058.1.

——, S. Zhong, W. E. Heilman, J. J. Charney, and X. Bian, 2018: A numerical study of atmospheric perturbations induced by heat from a wildland fire: Sensitivity to vertical canopy structure and heat source strength. *J. Geophys. Res. Atmos.*, **123**, 2555–2572, https://doi.org/10.1002/2017JD027904.

——, J. J. Charney, S. Zhong, W. E. Heilman, X. Bian, J. L. Hom, and M. Patterson, 2019: Evaluation of the ventilation index in complex terrain: A dispersion modeling study. *J. Appl. Meteor. Climatol.*, **58**, 551–568, https://doi.org/10.1175/JAMC-D-18-0201.1.

——, ——, ——, ——, ——, and T. O. Mathewson, 2020: A multiscale numerical modeling study of smoke dispersion and the ventilation index in southwestern Colorado. *Atmosphere*, **11**, 846, https://doi.org/10.3390/atmos11080846.

——, and Coauthors, 2022: Representing low-intensity fire sensible heat output in a mesoscale atmospheric model with a canopy submodel: A case study with ARPS-CANOPY (version 5.2.12). *Geosci. Model Dev.*, **15**, 1713–1734, https://doi.org/10.5194/gmd-15-1713-2022.

Lahm, P., 2020: The air quality and smoke management imperative. *NWCG Smoke Management Guide for Prescribed Fire*, J. Peterson et al., Eds., National Wildfire Coordinating Group, 5–10.

Larkin, N. K., and Coauthors, 2009: The BlueSky smoke modeling framework. *Int. J. Wildland Fire*, **18**, 906–920, https://doi.org/10.1071/WF07086.

Linn, R. R., S. L. Goodrick, S. Brambilla, M. J. Brown, R. S. Middleton, J. O'Brien, and J. K. Hiers, 2020: QUIC-fire: A fast-running simulation tool for prescribed fire planning. *Environ. Model. Software*, **125**, 104616, https://doi.org/10.1016/j.envsoft.2019.104616.

Liu, Y., S. Goodrick, and G. Achtemeier, 2018: The weather conditions for desired smoke plumes at a FASMEE burn site. *Atmosphere*, **9**, 259, https://doi.org/10.3390/atmos9070259.

——, and Coauthors, 2019: Fire behaviour and smoke modelling: Model improvement and measurement needs for next-generation smoke research and forecasting systems. *Int. J. Wildland Fire*, **28**, 570–588, https://doi.org/10.1071/WF18204.

——, and Coauthors, 2022: Smoke plume dynamics. *Wildland Fire Smoke in the United States: A Scientific Assessment*, D. L. Peterson, S. M. McCaffrey, and T. Patel-Weynand, Eds., Springer, 83–119.

Miller, C., S. O'Neill, M. Rorig, and E. Alvarado, 2019: Air-quality challenges of prescribed fire in the complex terrain and wildland urban interface surrounding Bend, Oregon. *Atmosphere*, **10**, 515, https://doi.org/10.3390/atmos10090515.

Moeng, C.-H., and J. C. Wyngaard, 1989: Evaluation of turbulent transport and dissipation closures in second-order modeling. *J. Atmos. Sci.*, **46**, 2311–2330, https://doi.org/10.1175/1520-0469(1989)046<2311:EOTTAD>2.0.CO;2.

National Interagency Fire Center, 2019: Prescribed fire and acres by agency. National Interagency Fire Center, accessed 15 September 2023, https://www.nifc.gov/fire-information/statistics/prescribed-fire.

Noilhan, J., and S. Planton, 1989: A simple parameterization of land surface processes for meteorological models. *Mon. Wea. Rev.*, **117**, 536–549, https://doi.org/10.1175/1520-0493(1989)117<0536:ASPOLS>2.0.CO;2.

Pisso, I., and Coauthors, 2019: The Lagrangian particle dispersion model FLEXPART version 10.4. *Geosci. Model Dev.*, **12**, 4955–4997, https://doi.org/10.5194/gmd-12-4955-2019.

Pleim, J. E., and A. Xiu, 1995: Development and testing of a surface flux and planetary boundary layer model for application in mesoscale models. *J. Appl. Meteor.*, **34**, 16–32, https://doi.org/10.1175/1520-0450-34.1.16.

Powers, J. G., and Coauthors, 2017: The Weather Research and Forecasting Model: Overview, system efforts, and future directions. *Bull. Amer. Meteor. Soc.*, **98**, 1717–1737, https://doi.org/10.1175/BAMS-D-15-00308.1.

Ryan, K. C., E. E. Knapp, and J. M. Varner, 2013: Prescribed fire in North American forests and woodlands: History, current practice, and challenges. *Front. Ecol. Environ.*, **11**, e15–e24, https://doi.org/10.1890/120329.

Seto, D., C. B. Clements, and W. E. Heilman, 2013: Turbulence spectra measured during fire front passage. *Agric. For. Meteor.*, **169**, 195–210, https://doi.org/10.1016/j.agrformet.2012.09.015.

Skowronski, N. S., K. L. Clark, M. Duveneck, and J. Hom, 2011: Three-dimensional canopy fuel loading predicted using upward and downward sensing LiDAR systems. *Remote Sens. Environ.*, **115**, 703–714, https://doi.org/10.1016/j.rse.2010.10.012.

Solomos, S., and Coauthors, 2015: Smoke dispersion modeling over complex terrain using high resolution meteorological data and satellite observations – The Firehub platform. *Atmos. Environ.*, **119**, 348–361, https://doi.org/10.1016/j.atmosenv.2015.08.066.

Stohl, A., C. Forster, A. Frank, P. Seibert, and G. Wotawa, 2005: Technical note: The Lagrangian particle dispersion model FLEXPART version 6.2. *Atmos. Chem. Phys.*, **5**, 2461–2474, https://doi.org/10.5194/acp-5-2461-2005.

Stull, R. B., 1988: *An Introduction to Boundary Layer Meteorology*. Kluwer Academic, 666 pp.

USFS, 2022: Confronting the wildfire crisis: A new strategy for protecting communities and improving resilience in America's forests. USDA Forest Service Tech. Rep. FS-1187a, 25 pp., https://www.fs.usda.gov/sites/default/files/Confronting-Wildfire-Crisis.pdf.

van Wagtendonk, J. W., 2006: Fire as a physical process. *Fire in California's Ecosystems*, J. W. van Wagtendonk et al., Eds., University of California Press, 38–57.

Xue, M., K. K. Droegemeier, and V. Wong, 2000: The Advanced Regional Prediction System (ARPS) – A multi-scale nonhydrostatic atmosphere simulation and prediction model. Part I: Model dynamics and verification. *Meteor. Atmos. Phys.*, **75**, 161–193, https://doi.org/10.1007/s007030070003.

——, and Coauthors, 2001: The Advanced Regional Prediction System (ARPS) – A multi-scale nonhydrostatic atmosphere simulation and prediction tool. Part II: Model physics and applications. *Meteor. Atmos. Phys.*, **76**, 143–165, https://doi.org/10.1007/s007030170027.